Review of Scientific Instruments

A novel experimental chamber for the characterization of free-falling particles in volcanic plumes

Cite as: Rev. Sci. Instrum. **93**, 075105 (2022); https://doi.org/10.1063/5.0093730
Submitted: 30 March 2022 • Accepted: 20 June 2022 • Published Online: 08 July 2022
Published open access through an agreement with JISC Collections

Antonio Capponi, Steve J. Lane, Jennie S. Gilbert, et al.

Review of Scientific Instruments ARTICLE scitation.org/journal/rsi

A novel experimental chamber for the characterization of free-falling particles in volcanic plumes

Cite as: Rev. Sci. Instrum. 93, 075105 (2022); doi: 10.1063/5.0093730
Submitted: 30 March 2022 • Accepted: 20 June 2022 •
Published Online: 8 July 2022

Antonio Capponi,[1,a] Steve J. Lane,[1] Jennie S. Gilbert,[1] David G. Macfarlane,[2] Duncan A. Robertson,[2] and Mike R. James[1]

AFFILIATIONS

[1] Lancaster Environment Centre, Lancaster University, Lancaster LA1 4YQ, United Kingdom
[2] SUPA School of Physics and Astronomy, University of St Andrews, St Andrews, Fife KY16 9SS, United Kingdom

[a] **Author to whom correspondence should be addressed:** a.capponi2@lancaster.ac.uk

ABSTRACT

Volcanic plumes pose a hazard to health and society and a particular risk for aviation. Hazard mitigation relies on forecasting plume dispersion within the atmosphere over time. The accuracy of forecasts depends on our understanding of particle dispersion and sedimentation processes, as well as on the accuracy of model input parameters, such as the initial particle size distribution and concentrations of volcanic particles (i.e., volcanic ash) in the atmosphere. However, our understating of these processes and the accurate quantification of input parameters remain the main sources of uncertainty in plume dispersion modeling. It is usually impractical to sample volcanic plumes directly, but particle sedimentation can be constrained in the laboratory. Here, we describe the design of a new experimental apparatus for investigating the dynamics of free-falling volcanic particles. The apparatus can produce a sustained column of falling particles with variable particle concentrations appropriate to a volcanic plume. Controllable experimental parameters include particle size distributions, types, and release rates. A laser-illuminated macrophotography system allows imaging of in-flight particles and their interactions. The mass of landing particles is logged to inform deposition rates. Quantitative measurements include particle morphology characterization, settling velocities, flow rates, and estimation of concentrations. Simultaneous observations of particle interaction processes and settling dynamics through direct control over a wide range of parameters will improve our parameterization of volcanic plume dynamics. Although the apparatus has been specifically designed for volcanological investigations, it can also be used to explore the characteristics of free-falling particle columns occurring in both environmental and industrial settings.

I. INTRODUCTION

Volcanic plumes are mixtures of volcanic gases, volcanic particles, and air entrained from the atmosphere within which the eruptions take place. Depending on their dimensions, erupted particles are classified as volcanic blocks and bombs (diameter, d, >64 mm), lapilli (2 mm < d < 64 mm), coarse-grained ash (64μm < d < 2 mm), and fine-grained ash (d < 64 μm). Blocks and bombs are usually removed from the column within the initial eruptive phases and settle close to the volcano along ballistic trajectories. However, the smaller particles (d < 100 μm) are dispersed into the atmosphere in volcanic plumes and volcanic clouds and are transported at distances that can reach global scale. Once in the atmosphere, ash dispersal and sedimentation processes are mainly controlled by atmospheric conditions (e.g., wind directions, atmospheric turbulence, temperature, humidity) and internal plume dynamics, such as settling velocity and aggregation processes (Sparks *et al.*, 1997). Settling velocity is a complex function of particle size distribution (PSD), density, and shape (Wilson and Huang, 1979). Aggregation promotes the adhesion of individual particles into larger clusters (i.e., aggregates), settling at higher velocities than those of the individual particles (Lane *et al.*, 1993). Both settling and aggregation processes have a primary control on the ash residence time in the atmosphere and, therefore, on its dispersion. Atmospheric residence

time is of primary concern for aviation due to risks to aircraft on encountering airborne ash ranging from instrumentation damage up to engine failure (Casadevall, 1994). The level of disruption a volcanic plume can have on aviation was dramatically demonstrated by the Icelandic eruption of Eyjafjallajökull (April and May 2010; Mazzocchi *et al.*, 2010). Volcanic particle fallout in areas both proximal and distal to the volcano poses a hazard for health, society, and infrastructure. Chronic respiratory symptoms resulting from exposure to ash, contamination of water supply and soil, building collapse, and general damage to infrastructure are only some of the well-documented consequences of the impact of plumes on society (Durant *et al.*, 2010; Baxter and Horwell, 2015).

Mitigating hazard from volcanic plumes requires that we accurately detect plume particle concentrations and PSDs, mainly using

TABLE I. Laboratory experiment studies of particles in volcanic plumes.

References	Focus	Ash particle size (mm)	Experimental method
Wilson and Huang (1979)	Settling velocity of ash particles	0.3–1.5	Fall of groups of particles released in a vertical metal tube
Lane *et al.* (1993)	Setting velocity of ash aggregates	1–10	Fall of particles and constructed aggregates within a liquid-filled cylinder
Schumacher (1994)	Dry aggregation	<0.25	Electrostatic powder coating device used on falling ash
Gilbert and Lane (1994)	Wet aggregation	<0.3	Particles introduced in a recirculating wind tunnel
Schumacher and Schmincke (1995)	Wet aggregation	0.35–2	Electrostatic powder coating device used on falling ash
James *et al.* (2000)	Particle charging mechanism	<0.1	Falling ash produced by breaking cm-sized pumices
James *et al.* (2002; 2003)	Dry aggregation	< ~200	Falling ash produced by breaking cm-sized pumices
Dellino *et al.* (2005)	Settling velocity of ash particles	<0.05–4	Free-fall experiments of volcanic ash
Durant *et al.* (2008)	Ice nucleation properties of ash particles	<1	Single-particle ice nucleation freezing experiments
Kueppers *et al.*, (2011)	Wet aggregation	0.09–0.125	Aggregation formation by fluidized bed spray
Taddeucci *et al.* (2011)	Aggregation mechanism and settling velocity	0.125–3	Free-fall experiments of individual volcanic ash particles
Van Eaton *et al.* (2012)	Wet aggregation (ice and water)	<1.4	Vibratory pan aggregation technique
Telling and Dufek (2012)	Wet aggregation	0.106–0.25	Jet of volcanic ash in a humidity-controlled chamber
Telling *et al.* (2013)	Wet aggregation	0.09–0.10	Release of ~100 particles in a controlled atmospheric (humidity and pressure) chamber
Cimarelli *et al.* (2014)	Electrification of volcanic jets	0.09–0.5	Shock-tube experiments
Del Bello *et al.* (2015)	Dry aggregation and disaggregation mechanisms	<0.032–0.09	Particles kept in turbulent suspension by airflow
Mueller *et al.* (2016; 2017)	Wet aggregation	<0.05–210	Fluidized bed spray aggregation
Del Bello *et al.* (2017)	Settling velocity of ash particles	0.125–1	Free-fall experiments of volcanic ash
Del Bello *et al.* (2018)	Resuspension of volcanic ash	<0.063–0.25	Environmentally controlled recirculating wind tunnel
Gaudin and Cimarelli (2019)	Electrification of volcanic jets	0.09–0.3	Shock-tube experiments

remote sensing instruments, and forecast plume dispersion and evolution over time. To do so, an understanding of plume internal dynamics is fundamental, and, over the past few decades, laboratory experiments have played a central role in providing insight into some of these dynamics, focusing mostly on settling velocities and aggregation processes (Table I). Settling velocities and the complex influence of particle characteristics (shape, size, and density) have been constrained through particle free-fall experiments in fluids of known characteristics (Wilson and Huang, 1979; Lane *et al.*, 1993; Dellino *et al.*, 2005; Taddeucci *et al.*, 2011; and Del Bello *et al.*, 2017). If aggregation occurs, different types of aggregates may form depending on environmental conditions, fall velocities, the presence of a hygroscopic species, and electrostatic forces. Humidity, liquid bonding, chemistry of liquids coating ash surfaces are all parameters that may promote "wet" aggregation, as demonstrated by aggregation experiments in, e.g., recirculating wind tunnels and humidity-controlled chambers (Gilbert and Lane, 1994; Schumacher and Schmincke, 1995; and Telling and Dufek, 2012). In the absence of a liquid phase, "dry" aggregation may occur through a combination of electrostatic charging and differences in particle settling velocities (Schumacher, 1994; James *et al.*, 2002; and 2003). Recent ice nucleation experiments started to investigate the role of ash–ice interaction on aggregation mechanisms (Durant *et al.*, 2008; Hoyle *et al.*, 2011; Steinke *et al.*, 2011; and Van Eaton *et al.*, 2012). Ash electrification within ash-rich plumes is also responsible for the generation of volcanic lightning, recently recreated for the first time in a laboratory environment through shock-tube experiments (Cimarelli *et al.*, 2014; Gaudin and Cimarelli, 2019).

Knowledge of particle sedimentation and aggregation processes is critical for the development of models for forecasting plume dispersal and sedimentation. Outputs of dispersion models are often coupled with remote sensing data to produce advisories for airspace regions that forecast ash concentrations that may pose a risk to aviation and society. However, forecasts tend to underestimate ashfall in proximal areas and overestimate concentrations in the distal plume (Brown *et al.*, 2012; Folch, 2012). Indeed, models are still hampered by uncertainties, due to both an incomplete understanding of aggregation and settling processes and a lack of knowledge of the volcanological input parameters that include mass eruption rate and plume height, particle size distribution, and concentration (Folch, 2012). Although the quantification of these parameters is challenging, ground-based radar offers a means for deriving them remotely by measuring ash reflectivity within the plume. However, the available radars are mainly designed for meteorological observations, and their use for estimating volcanic plume parameters is limited because the effects of particle sizes and concentrations are ambiguous at a single frequency, requiring assumptions on one of these parameters. To resolve this ambiguity, a new close range, low power, continuous wave radar has been recently designed to simultaneously characterize falling volcanic ash in a laboratory-controlled environment at three different frequencies (10, 35 and 94 GHz; Macfarlane *et al.*, 2021). A laboratory calibration of radar backscatter from falling ash at three different radar frequencies is the crucial step for developing a multi-frequency radar reflectivity model and an inversion algorithm able to determine simultaneously and independently plume PSDs and concentrations. We have, therefore, developed a new ashfall chamber, to be used together with the radar, to characterize the backscatter properties of falling volcanic ash by measuring reflectivity of ash within a sampling volume at three different radar frequencies. The chief design considerations for the chamber were the ability to (1) create a controlled column of free-falling particles that could be maintained for tens of seconds, (2) produce particle concentrations within the experimental column that are similar to a volcanic plume, and (3) vary experimental parameters such as PSDs and particle type.

Although the apparatus has been developed for measuring the radar backscatter properties of volcanic ash, it also represents a considerable step forward for the characterization of free-falling particle columns. Despite the advances over the last three decades, we are yet to fully understand the physical and chemical processes involved in particle aggregation and settling and the control that parameters such as particle morphology, collisions, air entrainment, electrical charging, and liquid layers on particle surfaces have. Furthermore, the methodology for most previous laboratory experiment investigations (Table I) was designed for addressing one specific process, often within a limited parameter space. In contrast, the ability to create a repeatable and sustained column of falling particles of known characteristics paves the way to a wider range of investigations. The chamber's unique features allow the characteristics of a falling column of particles (e.g., including aggregation, sedimentation, collision, particle-entrained air interaction) to be observed and quantitatively measured by a variety of instruments, over a wide parameter space. Furthermore, devices that are routinely used for characterizing volcanic plumes (e.g., radar, lidar, hydrometers or thermal infrared instruments) have not always been systematically calibrated for the detection of volcanic ash. Such calibrations could be done using this chamber, to refine ash retrievals from inversion of remote sensing observations.

Here, we describe the components, operation, and default instrumentation of the apparatus aimed at volcanological processes. Nonetheless, the apparatus is sufficiently flexible that it can be used for any other airborne particle settling environment common in both environmental and industrial settings, such as pneumatic conveying transport, material handling, and falling streams of bulk material and powders (e.g., food and pharmaceutical industry, and mining processes).

II. APPARATUS

We designed and assembled the new experimental fall chamber in the Physical Volcanology Laboratory of the Lancaster Environment Centre at Lancaster University in the UK. The apparatus includes two main components: (1) a particle dispersion system of dimensions 0.55 × 0.55 × 0.55 m, comprising a mechanical release for the particles and a sieving mechanism for their dispersion, and (2) an instrumented fall chamber, of dimensions 2 × 1.45 × 1.45 m, connected at its top to the dispersion system. The entire apparatus is supported by an aluminum structure, fixed to a 1.45 × 1.45 × 0.02 m steel base (Fig. 1).

A. Particle dispersion system

The particle dispersion system has been designed explicitly to generate a column of particles with a constrained diameter of

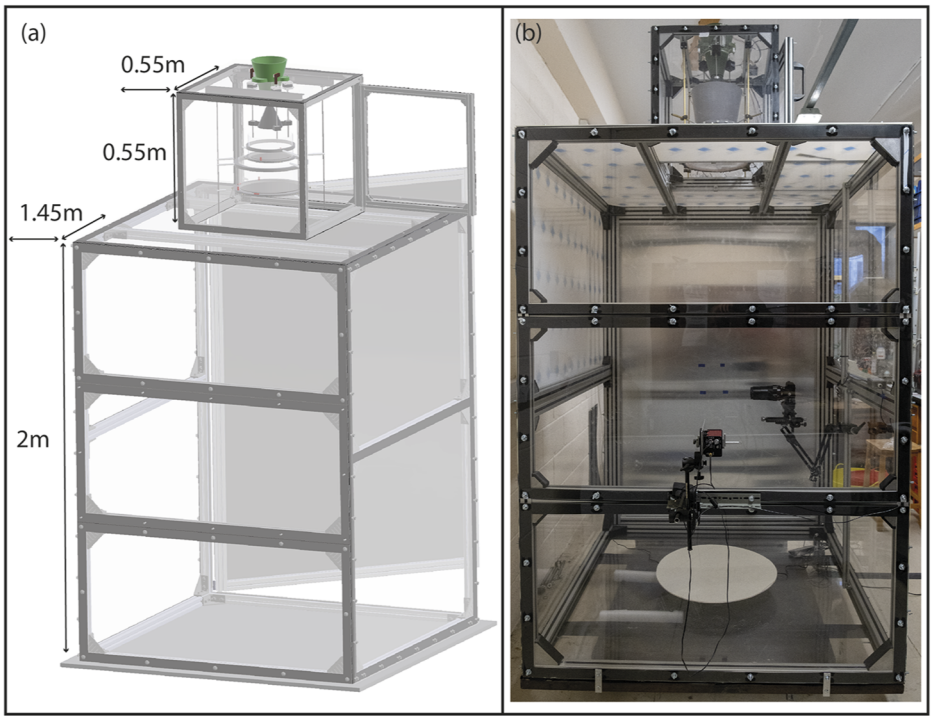

FIG. 1. (a) Technical drawing of the experimental apparatus and (b) view of the assembled apparatus in the Physical Volcanology Laboratory at Lancaster University, UK.

~30 cm. Such a diameter provides a volume of falling particles over time that ensures that the sampling volume of the triple-frequency radar is entirely within the column (see Macfarlane *et al.*, 2021, for details of the radar design). The particle dispersion system comprises two main components: (1) a mechanical particle release system, which serves as a means for releasing the material either at a fixed or variable release rate, and (2) a vibrating sieves system, which horizontally scatters the released particles over an area of ~0.07 m^2, generating a well-constrained column of free-falling particles.

1. Release system

The release system is a custom-designed conical valve. It allows a uniform mass flow discharge of particulates of different types (e.g., volcanic ash, artificial particles, powder mixes) by overcoming particle handling problems such as obstruction and size segregation. It comprises a holding hopper for the material, sealed by a vibrating cone that, when lowered, initiates the particle release through an annular gap. Three linear actuators control the cone movement, with the support of a homing system for setting their origin coordinates (Fig. 2). Both the hopper and the cone were 3D printed to specification.

The holding hopper is funnel-shaped, 216 mm tall, with a larger diameter of 160 mm at the top, and 60 mm at the bottom. It is bolted to the top plate of the release system, and it can hold sufficient material for releases lasting from a few seconds up to a few tens of minutes, depending on the particle size distribution. Within the hopper, 45 mm from its base, an Eccentric Rotating Mass (ERM) Precision Microdrives vibration motor (model 307-103, diameter 9 mm, length 25 mm) sits inside a cavity, held in place by a bracket to ensure a secure contact between the motor and the hopper [Figs. 2(c), 2(d), and 2(e)]. The ERM motor is fully encapsulated in a water- and particle-tight case, sealed by a ring of epoxy adhesive. Therefore, it is ideal for applications in environments with particles or debris.

The outlet of the hopper is kept sealed by a cone with a base diameter of 120 mm and a height of 135 mm. It is hollow only from its base up to 80 mm of height, and a mini vibration motor is inserted in its tip [Precision Microdrives 306-10H, diameter 7 mm, length of 25 mm; Figs. 2(c), 2(d) and 2(e)].

Three Nanotec non-captive linear actuators NEMA17 (LA421S14–B-UIEV) control the cone movements. These bipolar actuators have a maximum speed of 100 mm/s and a resolution of 0.025 mm/STEP. Each motor can bear a load of 10 kg, therefore, allowing a theoretical maximum particle load of 30 kg. The maximum speed for the current application has been capped at 80 mm/s. Such speed allows a fast opening of the annular gap for any of the desired range of particle release rates, while reducing unwanted misalignment among the motors that may be caused during high-speed movements. Three individual Texas Instruments DRV8825 stepper motor drives, with a maximum output capacity of 45 V and up to 2.2 A current output per coil, drive the actuators. Each drive offers up to 1/32 micro-stepping, allowing smooth and high-resolution movements. The current limit for the motors is set using the onboard voltage regulator on each drive and, for this application, we decided for a reference voltage of 0.5 V. The drives are mounted on an Arduino Shield on which three dip switches are available for setting their resolution (i.e., step size) using jumper

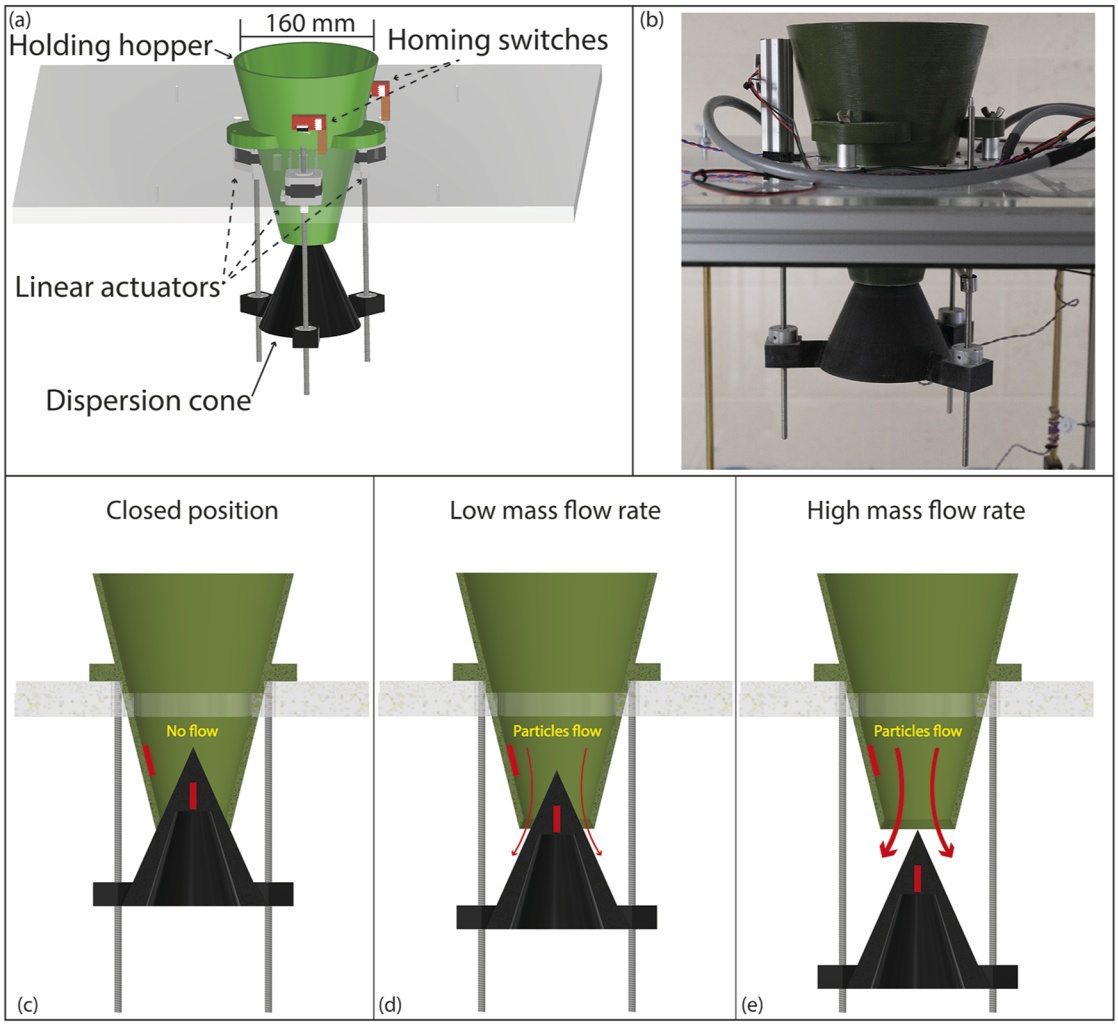

FIG. 2. (a) Technical drawing of the release system. (b) Close-up view of the assembled release system in the laboratory. Examples of the cone locked in (c) closed position and sealing the hopper, (d) low particle release rate position, and (e) high particle release rate position. A wide range of release rates can be achieved in-between the minimum and maximum release rates, by locking the cone at different heights. The cone position can also be varied during a single release process, allowing experiments to run at variable release rates. Inside the hopper and in the tip of the cone, two vibration motors stimulate the flow [red symbols in (c), (d), and (e)].

wires. For this application, all drives are set to 1/16 micro-step resolution. Two drives are configured as x- and y-axes, while the third drive is set to clone the y-axis. The Shield is connected to an Arduino Uno R3 board with the open source GRBL (v1.1, https://github.com/grbl/grbl) loaded into it as controller. The default GRBL configuration is uploaded to the board using Arduino software IDE. Specifically designed for computerized numerical control (CNC) milling machines, GRBL offers excellent movements, timing, and motor calibration controls. Commands to the motors are sent via lines of G-code, which is one of the most widely used programming language for CNC machines, using Universal G-code Sender (UGS, https://github.com/winder/Universal-G-Code-Sender). UGS is an open source Java based G-code platform, used for interfacing with a variety of CNC controllers like GRBL. The motors can be programmed either to move the cone a certain distance and close it again after a certain time, releasing the particles at a single flow rate for a fixed duration, or to automatically move the cone to different heights at different time steps, therefore, varying the flow rate during a single release period. The actuators are mounted to the top plate within the dispersion chamber. The rods from the motors connect to the cone by means of three 50-mm-long horizontal supports extending from the base of the cone. With the exception of the anchorage point for the rods, these brackets are triangular-shaped, so that particles will not accumulate on them during the release. Two end-stop switches, located outside the dispersion chamber, are used for both homing the motors (for the x- and y-axes, while the third motor clones the homing cycle of the y-axis) and as a safety measure. The homing allows the

motors to be precisely positioned: Each time the Arduino board is powered on, the motors move the cone until the rods hit the switches and then 0.6 mm down from the homing point, sealing the hopper and setting origin coordinates for the three motors. After the homing cycle, if the motors attempt to move the cone to a higher position than the closing one, therefore, hitting the switches, the system automatically shuts down. We used UGS to set all the main motors parameters in GRBL for both the homing settings and axes travel resolution. As one of the motors clones the y-axis, we disabled the z-axis limit switch in GRBL. Motors speed for the homing cycle is capped at 1.5 mm/s, allowing a precise alignment with the end-stop switches. We also calibrated each motor individually, to precisely adjust its step/mm and set the correct x- and y-axes travel resolution in GRBL (resulting, for this application and the current setup, in 669.5 and 663.4 step/mm for x- and y-axes, respectively).

Once the hopper is filled, the particles will remain undisturbed and without any additional transportation or disturbance until the release process. By moving downward from its closed position [Fig. 2(c)], the cone creates an annular gap allowing particles to exit the hopper under mass flow. At that point, particles in the same cross section will move at the same time, flowing "first in, first out,"

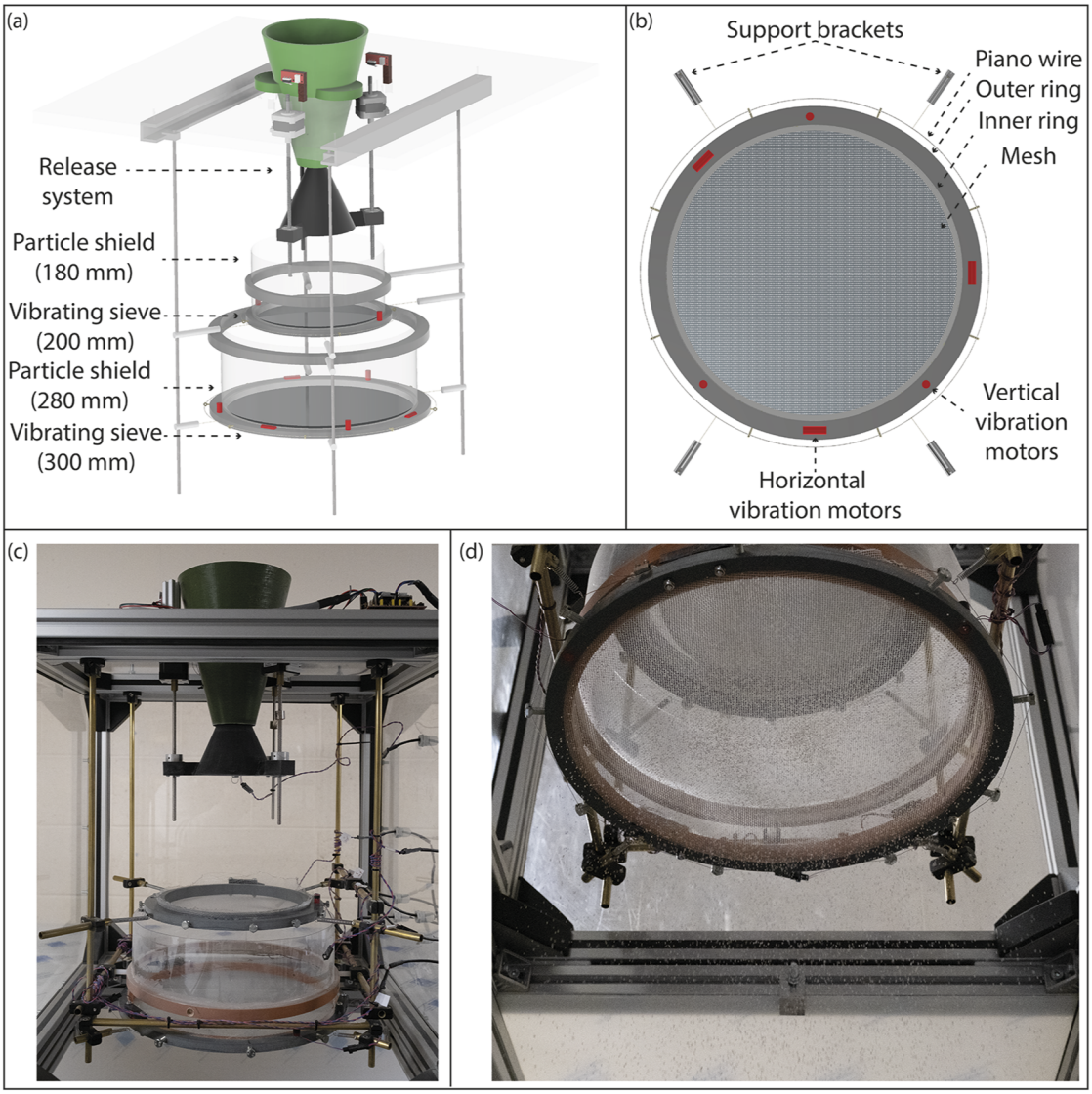

FIG. 3. Technical drawing of (a) the vibrating sieve system and (b) the 300 mm suspended vibrating sieve. The same structure shown in (b) applies to the 200 mm vibrating sieve, but only two vibration motors are mounted on the smaller ring (with slots already available for adding two additional ones if needed). (c) Close-up view of the vibrating sieves, assembled with the release system on top of the fall chamber, and (d) example of particles being dispersed by the 30 cm vibrating sieve and forming a falling column.

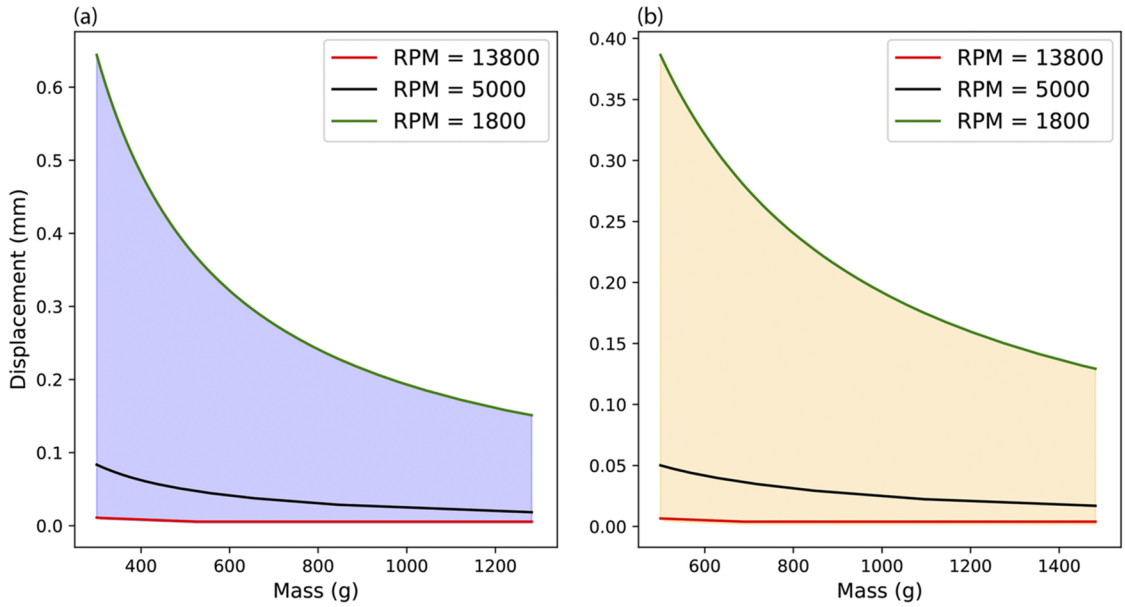

FIG. 4. Theoretical vibration displacements (mm, y-axis) for the vibration motors, as a function of mass (g, x-axis), for the sieve of (a) d = 200 mm and (b) d = 300 mm. The displacement varies depending on the revolutions per minute (RPM) of the motors (green line = 1800 RPM, black line = 5000 RMP, red line = 13 800 RPM) and the shaded areas indicate the displacement ranges achievable with the current setup.

avoiding segregation processes and flow inhomogeneity. Depending on the release rate and particle size distribution, both the vibration motors in the hopper and inside the tip of the cone may further stimulate the flow, disturbing the material in the hopper and promoting the release, while reducing the risk of blockages. When in use, the motors are activated simultaneously with the actuators, to avoid pre-release segregation of the material. The lower the cone moves, the higher the particle release rate [Figs. 2(d) and 2(e)].

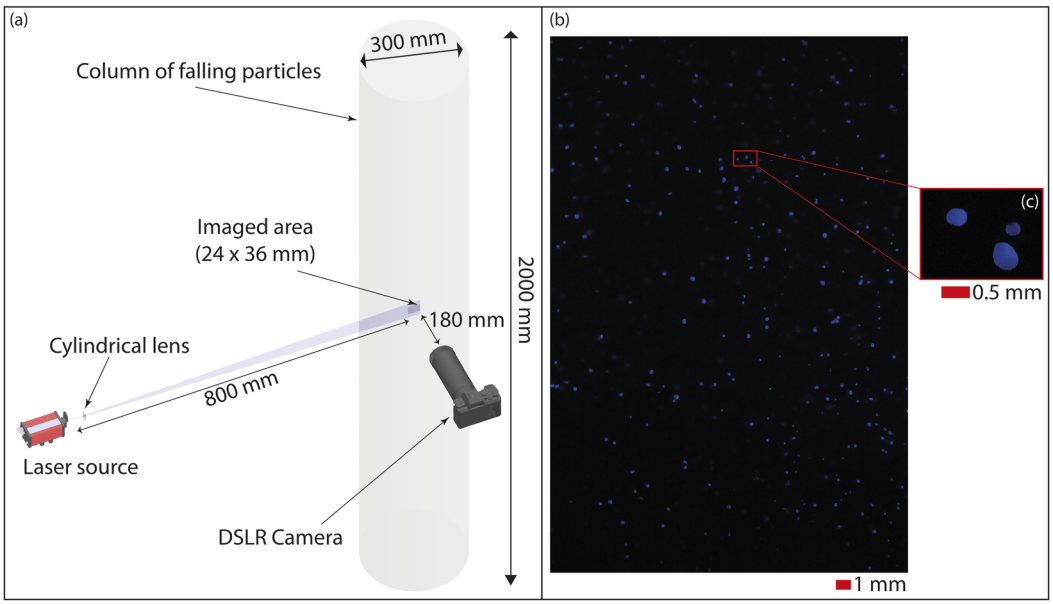

FIG. 5. (a) Falling particles are imaged in the middle of the column over a 24 × 36 mm^2 area. A cylindrical lens generates a laser line from the laser beam, illuminating the entire imaged area and camera depth of field. (b) Example of in-flight particles (grain size: 0.25–0.5 mm) imaged by the camera (exposure: 1/200 sec at f/8, ISO 8000). (c) Details of laser-illuminated particles.

2. Vibrating sieves system

The vibrating sieves system comprises two stacked circular vibrating sieves of different diameters (Fig. 3), whose function is to gradually distribute the released particles in a horizontal fashion, ultimately creating a column ~300 mm in diameter of particles falling within the main chamber [Fig. 3(d)]. Once lowered, the dispersion cone disperses the particles on a larger area (0.012–0.02 m^2). Then, the particles first hit the smaller sieve (internal d of 200 mm), and then a second larger one (internal d of 300 mm). Two particle shields (between the cone and the first sieve, and in-between the two sieves) constrain the fall of particles on the outer edges of the flow, so that the entire mass of released particles falls onto the meshes.

Each vibrating sieve consists of two concentric rings, holding a nylon mesh in tension. The mesh aperture varies, depending on the particle size distribution. The outer rings accommodate either two (smaller mesh) or six (larger mesh) Precision Microdrives motors (model 307-103). All the motors are fully enclosed within the rings, to ensure secure mounting and allow the full displacement to be transferred from the motors to the mesh. Half of the motors on each ring are oriented horizontally, while the others are in the vertical position [Figs. 3(a) and 3(b)].

The vibration displacement varies depending on the mass of particles present on the mesh at any given time during a release (Fig. 4). As the efficiency in vibration decreases with increasing mass, the number of active motors on each sieve ensures that sufficient displacement can be transmitted to the system to distribute the material homogenously over the desired area. Running all the motors at fixed revolutions per minute (RPM), regardless of the mass flow rates, may cause very large displacements. In such cases, the particles on top of the mesh may not be able to either disperse efficiently or pass through the mesh. Reducing the number of active motors and adjusting their voltages—hence the speed—results in smaller displacements. The combination of number of active motors, their running parameters, and orientations are chosen depending on the mesh aperture and experimental mass flow rate, so that ultimately all particles pass through the meshes after being dispersed onto them.

To suspend the meshes, a ring of piano wire (d 0.0025 mm) surrounds the vibrating sieves, supported by a series of eyehooks screwed to the sides of the outer rings. Four springs are anchored to the piano wire. The springs, in turn, connect to four brackets of adjustable length connected to a support structure (Fig. 3). Once the meshes are centered below the cone and at the correct height, the brackets are used to extend the springs and tension the piano wire so that the sieves are securely kept in suspension. This system minimizes dissipation of the vibrations within the supporting frame and the rest of the apparatus and maximizes the efficiency of the motors.

B. Instrumented fall chamber

The main fall chamber (Fig. 1) is where the free-fall of particles occurs in a draught-proof environment, under laboratory temperature and humidity conditions. A ThermoPro TP55 thermo-hygrometer (temperature range: −30 to 60 ± 0.5 °C; humidity range: 10%–99%, ±2%) allows us to monitor temperature and humidity conditions, measuring current temperature and humidity values, 24 h high/low records, and trends for both temperature and humidity conditions. One side of the chamber is a 1.92 × 1.32 m^2 door to allow easy access to the interior of the chamber each time an experiment is complete. The chamber is supported by 45 × 45 mm^2 aluminum strut profiles. The use of these assembly elements allows easy modification of the chamber, as more struts can be added and used to support a variety of instruments. On the front, two horizontal struts create three viewing windows, sealed by three removable Plexiglass panels. Their heights are adjustable by sliding the supports at the desired level and support instrument installation at different levels (e.g., the current windows provide three measurement heights for radar observations). All the panels, except for the

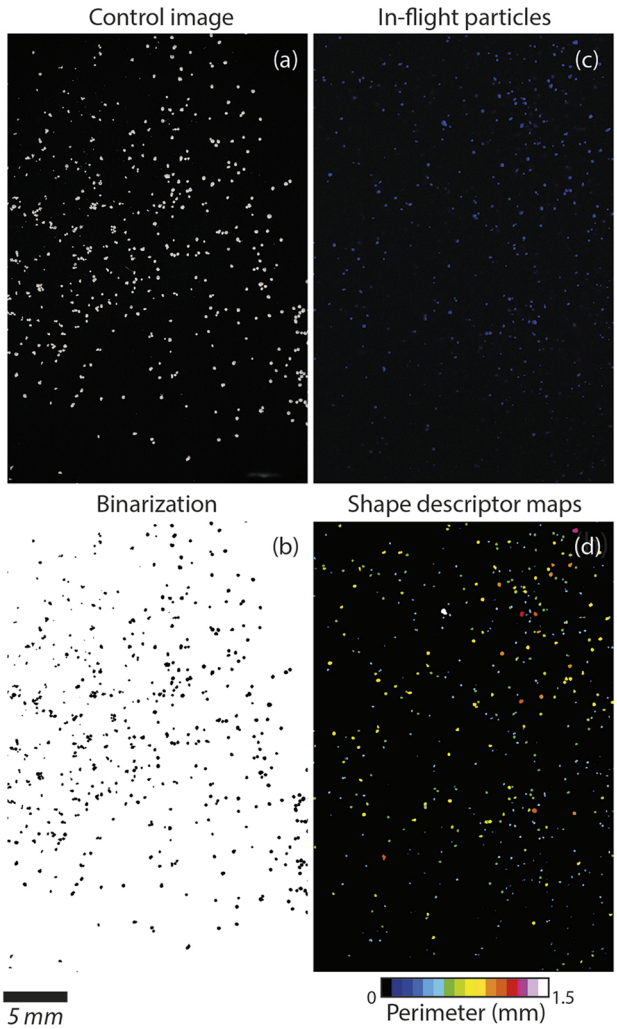

FIG. 6. Example of a control image for PSD3 (a) before post-processing and (b) after thresholding and binarization in ImageJ. Example of laser-illuminated in-flight particles for PSD3 (c) before and (d) after post-processing. (d) The color-coded image represents an example of shape descriptor map, showing variations in particle perimeters. Similar maps are created for all measured parameters, for both the control and in-flight particle images. The same scale bar applies to all images.

TABLE II. Summary of experimental parameters for test experiments and release characteristics.

PSD (mm)	Density (kg/m^3)	Mesh aperture (mm)	Cone opening range (mm)	Release rate range (g/s)	Release duration (s)[a]	Modal d (mm)[b] Low	Med	High	Control modal d (mm)[c]	Mean v_t (m/s)[b] Low	Med	High
PSD1 (0.5-1)	500 (±150)	1.25–1	2.8–10	1.6–33	7–170	0.53	0.64	0.58	0.54	2	1.95	2.25
PSD2 (0.25-0.5)	700 (±80)	1–0.56	1.5–9	2–30	9–148	0.29	0.29	0.30	0.28	1.23	1.53	1.75
PSD3 (0.1-0.3)	800 (±80)	0.56	0.5–4	0.9–11	22–200	0.16	0.15	0.14	0.17	1.14	1.16	0.93
PSD4 (0.04-0.125)	1150 (±300)	0.2	0.5–3	0.5–6	32–130	0.05	0.05	0.05	0.05	0.45	0.67	0.42

[a]Release duration for 300 g of particles for PSD1, 2, and 3, and 150 g for PSD4.
[b]From data for low, medium, and high release rates shown in Figs. 9(d) and 10 (v_t).
[c]From control data shown in Fig. 9.

access door, are optically clear and bolted to the supporting struts, with a 4-mm-thick rubber seal sandwiched between the panels and the supports. The door panel comprises a 2-mm-thick aluminum sheet. The default-installed instrumentation comprises a mass scale, to log deposit accumulation, and a laser-illuminated imaging system.

1. Mass logging

A high-resolution balance Kern PCD 10K0.1 is located at the bottom of the chamber to measure deposit accumulation. The balance has a maximum weighing capacity of 10 kg (with a measurement precision of 0.1 g) and it communicates with a control PC over an RS232C data interface cable. A container sufficiently large (570 mm in diameter and 160 mm high) to accommodate the settling particles is securely fixed to the 160 × 160 mm^2 weighing plate via a circular connecting plate 600 mm in diameter. The connection is designed to minimize movements and vibrations caused during particle release that may affect the accuracy of the measurements. The balance has a removable display so that operations can be carried out easily without interfering with the container, especially during the taring process. For data logging, measurements are set to percent determination. Before each experiment, the mass of particles to release is weighed, saved as a reference weight corresponding to 100%, and then removed. During the release, the percentage values of settling particles are sent continuously to the PC. The data are logged using a custom Python data logging script that automatically converts the percentage values in mass based on the reference weight, plots the settled mass over time, and stores the data for further data processing.

2. Imaging system

In-flight particles are imaged using a Sony α7RIII mirrorless camera and a Voigtländer Macro Apo-Lanthar 110 mm F2.5 lens. The camera has a resolution of 42.4 megapixels (8000 × 5320 pixel)

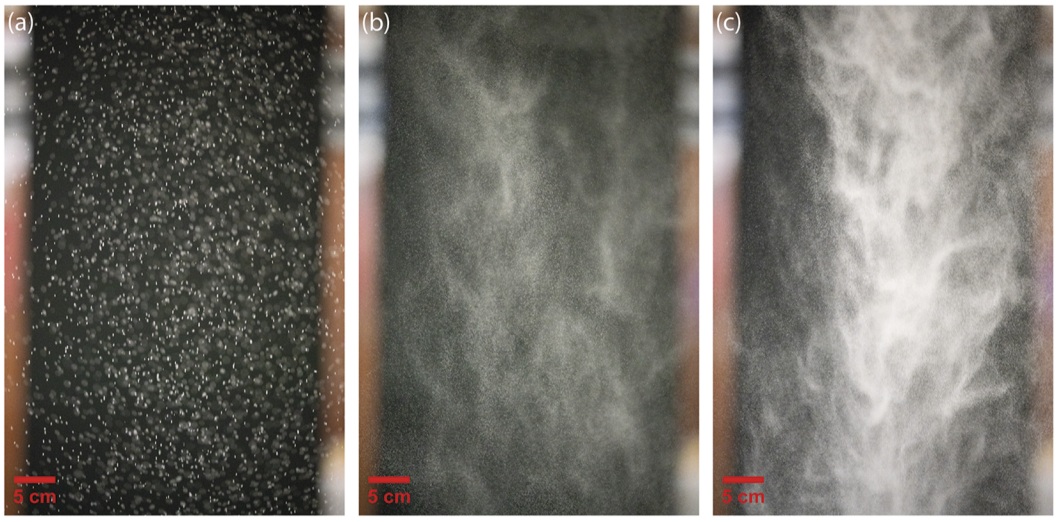

FIG. 7. Examples of falling particles within the chamber creating a column with a diameter of ~30 cm for (a) PSD1 and (b) PSD4 at low release rate, and of ~25 cm for (c) PSD4 at high release rate.

and allows recording of images at a maximum of 10 frames/s (fps) in short bursts. The imaged area is a region of 24 × 36 mm^2 in the center of the falling column, with the camera depth of field of 2 mm at magnification of either 1:1 from a working distance of 17 cm, or 1:2 from 34 cm, for an imaged area of 48 × 72 mm^2. The camera connects to the control PC via a USB Type-C and is fully controlled via the Sony proprietary software, Edge. Images are automatically transferred to the PC and stored in RAW format for post-processing.

A ThorLabs NPL45C nanosecond pulsed laser is used to create a light sheet illuminating the imaged area. A traditional light source or a strobe light would illuminate all the particles indiscriminately, both within and outside the very narrow lens depth of field. The presence of out-of-focus particles in the images may completely conceal the in-focus particles, especially in columns with high particle concentrations, potentially impeding image processing. By creating a light sheet illuminating just the camera depth of field, only the in-focus particles are imaged. The NPL45C has a wavelength of 450 nm, variable pulse width control (6–129 ns), pulse energy of 204 nJ, and peak power of 1600 mW (and also a typical optical power for a pulse of 129 ns—which is the pulse width in use). The laser pulses can be triggered either automatically (at 1, 5 or 10 MHz) or by connecting it, as in this application, to the camera. The laser beam has an asymmetric shape (major and minor axes of 2.1 and 1 mm, respectively, measured at 5 mm). From the beam, a 12.5 × 25 mm^2 cylindrical lens (Edmund Optics; effective focal lens of −50 mm, VIS 0° antireflection coating, wavelength range 425–675 nm) generates a light sheet with a thickness of ~3 mm and a height of 52 mm at the center of the column [from a distance of 800 mm; Fig. 5(a)]. Therefore, the laser light sheet covers the entire imaged area while illuminating only the particles within the camera depth of field [Figs. 5(b) and 5(c)].

III. APPARATUS TEST

We performed 225 particle releases to test the functionality of the apparatus, observe the main characteristics of the columns of falling particles, compare analysis of 1:1 images of in-flight particles with control images, measure particle settling velocities (v_t), and identify the ranges of release rates, duration, and their repeatability.

For all the tests we used, instead of volcanic ash, four known particle size distributions of Poraver expanded glass beads, which represent a good analog for ash: 0.5–1 mm (PSD1), 0.25–0.5 mm (PSD2), 0.1–0.3 mm (PSD3), and 0.04–0.125 mm (PSD4). Each size distribution was characterized by analyzing a population of ~1000 samples. Several high-resolution 1:1 control images of loose particles on a thin section were taken for each grain size using the Sony α7RIII camera [Fig. 6(a)]. All the images were binarized by thresholding [Fig. 6(b)] using ImageJ (Abràmoff *et al.*, 2004). Afterward, we used the ImageJ analysis toolbox to measure the following parameters: projected area, perimeter, major and minor axes of the particle best-fitting ellipsoids, Feret, and circularity. Images of in-flight particles were taken for most of the releases [Fig. 6(c)], and the same parameters measured for the control images were also measured for the falling particles [Fig. 6(d)]. The particles settled in a container secured on the mass balance, logging the deposition rate.

For the purpose of these tests, the same mass of particles (300 ± 30 g) was released for PSD1, PSD2, and PSD3. For PSD4, this was reduced to 150 (±30 g), although reference tests were also conducted with 300 g of particles. The cone opening was varied to achieve different constant release rates, and mesh aperture was changed depending on the PSD in use (Table II). To test the reproducibility of the releases and measurements, each release was repeated at least four times for all the parameters explored.

In all the tests, the particle flow through the annulus formed by the cone opening was well controlled and repeatable and there was complete discharge of the hopper without any blockage. Once the particles encountered the first and smaller vibrating mesh, they were dispersed across its area, and a column of particles (~20 cm in diameter) fell onto the second mesh, ultimately forming a well-constrained column of free-falling particles within the main chamber, with a diameter of ~30 cm [Figs. 3(d) and 7(a)]. The particle fall was steady, as shown by the log of deposit accumulation with time [Fig. 8(a)].

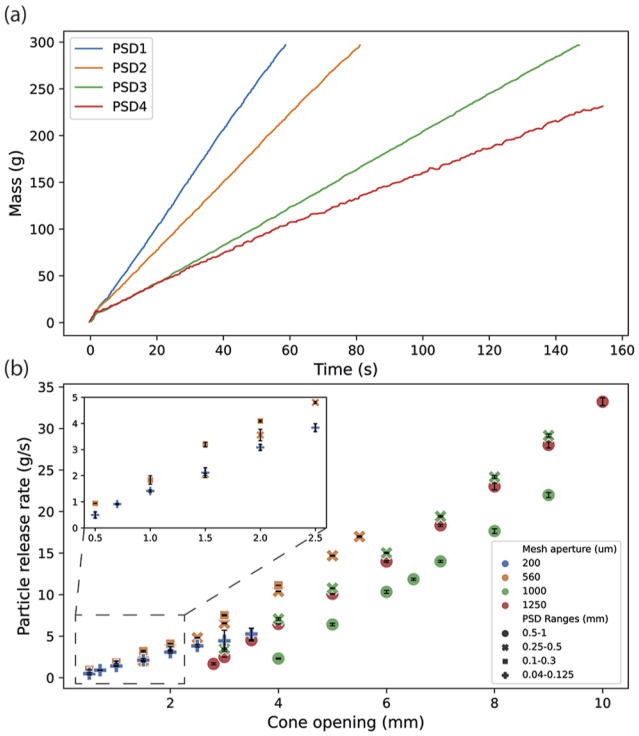

FIG. 8. (a) Particle mass deposition (g) measured by the mass balance over time (s) for different grain sizes: PSD1 (blue line), PSD2 (orange line), PSD3 (green line), and PSD4 (red line). In each case, 300 g of particles were released, but, for PSD4, only ~235 g deposited on the balance's container as particles departed from the main column depositing over all the chamber base. (b) Ranges of particle release rates (g/s), as a function of cone opening (mm) and particle size distributions (symbols). For some PSDs, different release rates are possible by varying mesh aperture (colors). Each point represents the mean value of the release rate over at least four different tests run under the same experimental conditions. The inset within (b) shows details for PSD2, 3, and 4 released within the 0.5–2.5 mm range of cone opening. Note that error bars are dominantly smaller than the symbol size.

The column of falling particles appeared well constrained throughout the entire release duration, especially for PSD1 [Fig. 7(a)] and PSD2, at both low and high release rates. As already observed during free-fall of particles (Cooper and Arnold, 1995; Ansart *et al.* 2009), the smaller the particles, the less constrained the column may become. This occurred at the highest release rate of PSD3 and at low-to-high release rates of PSD4. In such cases, although there was still the formation of a core column of ~30 cm in diameter, we observed the effects of particle–air interaction along the column edges. This was most noticeable in the case of the slower PSD4 release rates characterized by longer release duration. Any stream of free-falling particles induces an airflow around it. The smaller the particles, the more they are entrained into the airflow and separate from the main particle flow, creating a dispersion of small particles within the main chamber. The effects of this particle-driven convection are evident for PSD4. By logging the deposition rate, it was possible to quantify the effects of this separation: The total logged mass was always 5%–30% less than the released one, regardless of the release rate [Fig. 8(a)]. Furthermore, compared to the more homogeneous columns generated by larger PSDs [Fig. 7(a)], low release rates of PSD4 resulted in an inhomogeneous column of ~30 cm in diameter, where variations in particle concentration were clearly observable [Fig. 7(b)]. Particle concentrations in these clusters increased with an increase in release rate, while the diameter of the core column decreased to 25–27 cm [Fig. 7(c)].

Different and repeatable release rates were possible, by varying the cone opening and also the mesh aperture for the same PSD [Fig. 8(b)]. The lower and higher release rates were achieved with particles of size 0.04–0.125 mm (PSD4, 0.5 g/s) and 0.5–0.1 mm (PSD1, 33 g/s), respectively (Table II, Fig. 8(b). PSD4 was the particle size distribution characterized by larger variability in the measurements, due to the separation of smaller particles from the main flow, which was highly variable at any release rate [Fig. 8(b)].

Particle characteristics were quantified for imaged particles falling at different release rates and compared to the control images. In all cases, for each PSD, measurements from in-flight particles agree with the ones from the control images, demonstrating that the image system successfully captures the particle size distribution within the sampling volume. Modal values for particle areas obtained from in-flight particles at low, medium, and high release rates are all within error of the control images for PSD1, PSD2, and PSD3. For PSD4, modal values for the three release rates and the one from the control images match (Fig. 9; Table II). Similar agreements can be seen across the several parameters measured for each class of particles.

The image system was also used to acquire videos at 120 fps of falling particles in the center of the column. We used the video to track particles at different release rates. For each video, we measured the settling velocity, v_t, of ~200 particles using ImageJ and the MTrack J plug-in (Abràmoff *et al.*, 2004). Average overall velocities of 2, 1.5, 1, and 0.5 m/s characterize PSD1, PSD2, PSD3, and PSD4, respectively, with an increase from a minimum of 0.2 m/s to a maximum of 2.9 m/s as particle size increases from 0.04 to 1 mm. Within each PSD, the settling velocity varies depending on the particle size, with larger particles characterized by higher velocities (Fig. 10). For PSD1 and PSD2, particles released at higher rates seem to be characterized by higher velocities [Figs. 10(a) and 10(b)].

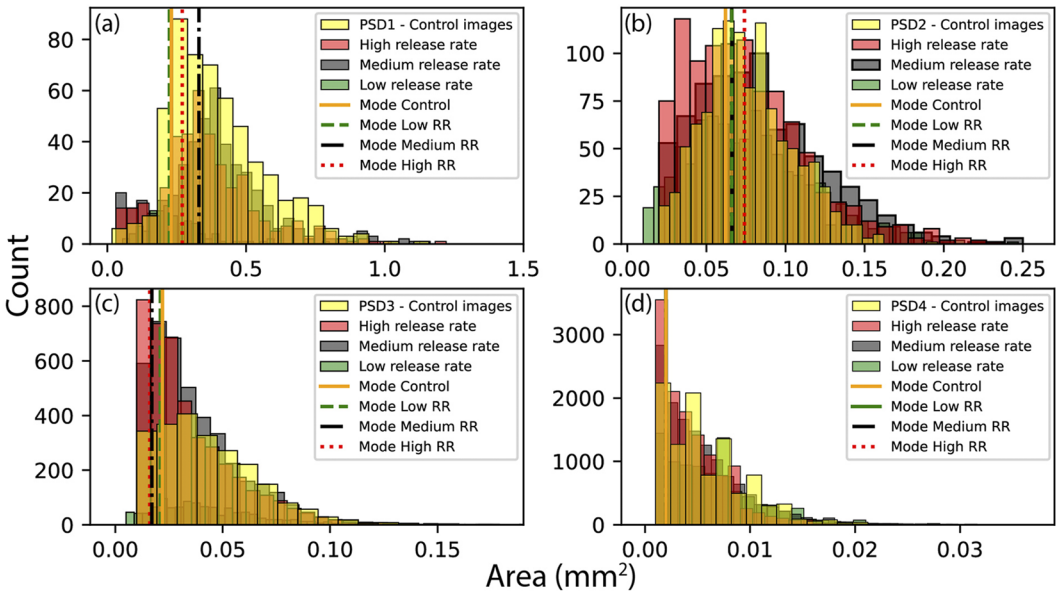

FIG. 9. Comparison of particle area distributions derived from analysis of control images (yellow histograms) and images of in-flight particles released at low (green histograms), medium (gray histograms), and high (red histograms) release rates (RRs), for (a) PSD1, (b) PSD2, (c) PSD3, and (d) PSD4. The vertical lines in each plot indicate the area modal values for the control images (orange), low release (green), medium release (black), and high release (red). In (d), the green, black, and red vertical lines are concealed behind to orange line because modal values for the three release rates and the one from the control images match.

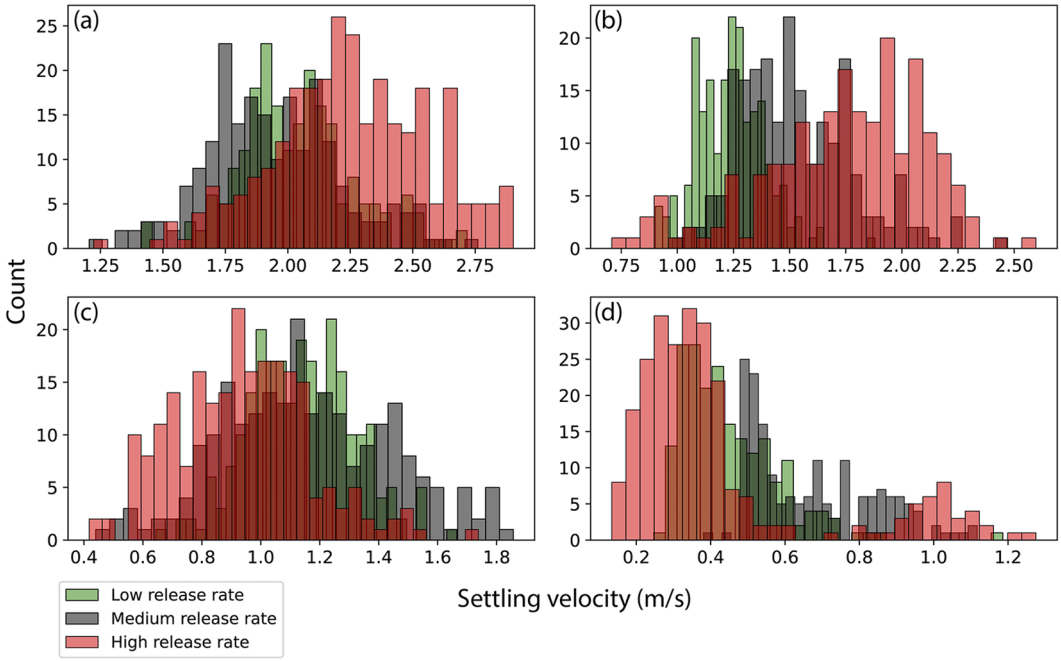

FIG. 10. Comparison of settling velocity (m/s) for (a) PSD1, (b) PSD2, (c) PSD3, and (d) PSD4, measured for different release rates: low (green), medium (red), and high (yellow).

This trend is not evident for PSD3 and PSD4 for which, in contrast, lower settling velocities characterize particles released at high release rates [Figs. 10(c) and 10(d)]. Furthermore, the velocity distribution for PSD4 seems to be bimodal, especially at high release rates [Fig. 10(d)], with modal values of 0.3 m/s and 1 m/s. This difference in ranges may indicate the possible presence of particle aggregation processes, with aggregates falling at higher velocities than those of the individual smaller particles, and particle-driven convection that may lead to differential settling.

For any PSD, the increase in the flow rate leads to an increase in particle concentrations within the column. The variation in the concentrations can be estimated in the experimental column. Particles pass through a circular cross-sectional area of ~0.07 m^2 at different release rates, from ~0.5 to ~33 g/s depending on PSDs, with average velocities of 0.5–2 m/s [Fig. 8(b) and Table II]. These ranges would put experimental concentrations in the region of 10^{-3} to 10^{-1} kg/m^3. The increase in particle concentrations within the column can also be estimated from the variation of the particle volume fraction, ϕ, measured in the images. ϕ is calculated as the total volume of all detected particles in one image [calculated as $V = (4/3)\pi(d_e/2)^3$, where d_e is the equivalent diameter of a sphere with the same area projected by a particle], divided by the control volume defined by the camera depth of field ($24 \times 36 \times 2$ mm^3). The value of ϕ ranges from 3×10^{-5} to 2×10^{-3} depending on the PSD, and it generally increases with an increase in the release rate. However, ϕ should not be treated as true concentration proxy (or as fixed value within a single release) because concentrations within the imaged volume may vary. These variations may occur due to interaction among the particles and between the particles and air within the main column and, for smaller PSDs, it may be strongly affected by particle-driven convection and the loss of smaller particles from the column.

IV. CONCLUSIONS

We present a new experimental apparatus, designed to investigate the dynamics of free-falling particles. The current design allows varying the particle type, size distribution, and mass flow rate. The release system is flexible such that it can be programmed to release particles at either a constant or varying rate. A laser-illuminated macrophotography imaging system allows particles to be imaged within the center of the falling column at a maximum magnification of 1:1. Preliminary experiments using different known particle size distributions demonstrate that it is possible to create repeatable experimental columns of falling particles characterized by varying release rates and concentrations that can be sustained over time. Data acquired from our tests allow characterization of the in-flight particles, such as morphological characterization, measurements of terminal fall velocities and mass flow rates, and estimations of particle concentrations. The apparatus has been designed for measuring the radar reflectivity of volcanic ash particles, using a newly developed triple-frequency radar. However, in addition to the specific volcanological application, it can be used to investigate the dynamics of free-falling particle columns that could occur in environmental and industrial situations, such as the dispersal of atmospheric pollutants, conveying of bulk materials,

unloading of powder tankers, transfer of food, and discharges of powders.

ACKNOWLEDGMENTS

The authors gratefully acknowledge the support from NERC, Grant No. NE/S005218/1, "*Radar-supported Next-Generation Forecasting of Volcanic Ash Hazard* (R4AsH)." The authors are grateful to David Lewis (Mechanical Workshop, Lancaster Environment Centre, Lancaster University) for his support in manufacturing several components required for the assembly and to the Department of Engineering (Lancaster University) for allowing the use of 3D printers and laser cutting machines.

AUTHOR DECLARATIONS

Conflict of Interest

The authors have no conflicts to disclose.

Author Contributions

Antonio Capponi: Conceptualization (equal); Data curation (lead); Formal analysis (lead); Investigation (lead); Methodology (lead); Resources (lead); Software (lead); Validation (lead); Visualization (lead); Writing – original draft (lead); Writing – review & editing (lead). **Steve J. Lane:** Conceptualization (equal); Funding acquisition (lead); Methodology (supporting); Writing – review & editing (supporting). **Jennie S. Gilbert:** Conceptualization (equal); Funding acquisition (lead); Methodology (supporting); Writing – review & editing (supporting). **David G. Macfarlane:** Methodology (supporting); Writing – review & editing (supporting). **Duncan A. Robertson:** Funding acquisition (lead); Writing – review & editing (supporting). **Mike R. James:** Conceptualization (lead); Funding acquisition (lead); Project administration (lead); Writing – review & editing (supporting).

DATA AVAILABILITY

The data that support the findings of this study are available from the corresponding author upon reasonable request.

REFERENCES

Abràmoff, M. D., Magalhães, P. J., and Ram, S. J., "Image processing with ImageJ," Biophotonics Int. **11**(7), 36–42 (2004).

Ansart, R., De Ryck, A., and Dodds, J. A., "Dust emission in powder handling: Free falling particle plume characterisation," Chem. Eng. J. **152**(2–3), 415–420 (2009).

Baxter, P. J. and Horwell, C. J., "Impacts of eruptions on human health," in *The Encyclopedia of Volcanoes* (Academic Press, 2015), pp. 1035–1047.

Brown, R. J., Bonadonna, C., and Durant, A. J., "A review of volcanic ash aggregation," Phys. Chem. Earth, Parts A/B/C **45–46**, 65–78 (2012).

Casadevall, T. J., "The 1989–1990 eruption of Redoubt Volcano, Alaska: Impacts on aircraft operations," J. Volcanol. Geotherm. Res. **62**, 301–316 (1994).

Cimarelli, C., Alatorre-Ibargüengoitia, M. A., Kueppers, U., Scheu, B., and Dingwell, D. B., "Experimental generation of volcanic lightning," Geology **42**(1), 79–82 (2014).

Cooper, P. and Arnold, P., "Air entrainment and dust generation from a falling stream of bulk material," KONA Powder Part. J. **13**, 125–134 (1995).

Del Bello, E., Taddeucci, J., Merrison, J. P., Alois, S., Iversen, J. J., and Scarlato, P., "Experimental simulations of volcanic ash resuspension by wind under the effects of atmospheric humidity," Sci. Rep. **8**(1), 14509 (2018).

Del Bello, E., Taddeucci, J., Scarlato, P., Andronico, D., Scollo, S., Kueppers, U., and Ricci, T., "Effect of particle volume fraction on the settling velocity of volcanic ash particles: Insights from joint experimental and numerical simulations," Sci. Rep. **7**(1), 39620 (2017).

Del Bello, E., Taddeucci, J., Scarlato, P., Giacalone, E., and Cesaroni, C., "Experimental investigation of the aggregation-disaggregation of colliding volcanic ash particles in turbulent, low-humidity suspensions," Geophys. Res. Lett. **42**(4), 1068–1075, https://doi.org/10.1002/2014gl062292 (2015).

Dellino, P., Mele, D., Bonasia, R., Braia, G., La Volpe, L., and Sulpizio, R., "The analysis of the influence of pumice shape on its terminal velocity," Geophys. Res. Lett. **32**(21), L21306, https://doi.org/10.1029/2005gl023954 (2005).

Durant, A. J., Bonadonna, C., and Horwell, C. J., "Atmospheric and environmental impacts of volcanic particulates," Elements **6**, 235–240 (2010).

Durant, A. J., Shaw, R. A., Rose, W. I., Mi, Y., and Ernst, G. G. J., "Ice nucleation and overseeding of ice in volcanic clouds," J. Geophys. Res.: Atmos. **113**, D09206, https://doi.org/10.1029/2007jd009064 (2008).

Folch, A., "A review of tephra transport and dispersal models: Evolution, current status, and future perspectives," J. Volcanol. Geotherm. Res. **235–236**, 96–115 (2012).

Gaudin, D. and Cimarelli, C., "The electrification of volcanic jets and controlling parameters: A laboratory study," Earth Planet. Sci. Lett. **513**, 69–80 (2019).

Gilbert, J. S. and Lane, S. J., "The origin of accretionary lapilli," Bull. Volcanol. **56**, 398–411 (1994).

Hoyle, C. R., Pinti, V., Welti, A., Zobrist, B., Marcolli, C., Luo, B., Höskuldsson, Á., Mattsson, H. B., Stetzer, O., Thorsteinsson, T., and Larsen, G., "Ice nucleation properties of volcanic ash from Eyjafjallajökull," Atmos. Chem. Phys. **11**(18), 9911–9926 (2011).

James, M. R., Gilbert, J. S., and Lane, S. J., "Experimental investigation of volcanic particle aggregation in the absence of a liquid phase," J. Geophys. Res.: Solid Earth **107**, 2191, https://doi.org/10.1029/2001jb000950 (2002).

James, M. R., Lane, S. J., and Gilbert, J. S., "Volcanic plume electrification: Experimental investigation of a fracture charging mechanism," J. Geophys. Res.: Solid Earth **105**, 16641–16649, https://doi.org/10.1029/2000jb900068 (2000).

James, M. R., Lane, S. J., and Gilbert, J. S., "Density, construction, and drag coefficient of electrostatic volcanic ash aggregates," J. Geophys. Res.: Solid Earth **108**, 2435, https://doi.org/10.1029/2002jb002011 (2003).

Kueppers, U., Auer, B., Cimarelli, C., Scolamacchia, T., and Dingwell, D. B., "Experimentally constraining the boundary conditions for volcanic ash aggregation," AGU Fall Meet. Abstr. **2011**, V51F–V2576.

Lane, S. J., Gilbert, J. S., and Hilton, M., "The aerodynamic behaviour of volcanic aggregates," Bull. Volcanol. **55**, 481–488 (1993).

Macfarlane, D. G., Robertson, D. A., and Capponi, A., "R4AsH: A triple frequency laboratory radar for characterizing falling volcanic ash," Proc. SPIE **11742**, 1174219 (2021).

Mazzocchi, M., Hansstein, F., and Ragona, M., "The 2010 volcanic ash cloud and its financial impact on the European airline industry," in *CESifo Forum* (München: ifo Institut für Wirtschaftsforschung an der Universität München, 2010), Vol. 11, p. 2.

Mueller, S. B., Ayris, P. M., Wadsworth, F. B., Kueppers, U., Casas, A. S., Delmelle, P., Taddeucci, J., Jacob, M., and Dingwell, D. B., "Ash aggregation enhanced by deposition and redistribution of salt on the surface of volcanic ash in eruption plumes," Sci. Rep. **7**(1), 45762–45769 (2017).

Mueller, S. B., Kueppers, U., Ayris, P. M., Jacob, M., and Dingwell, D. B., "Experimental volcanic ash aggregation: Internal structuring of accretionary lapilli and the role of liquid bonding," Earth Planet. Sci. Lett. **433**, 232–240 (2016).

Schumacher, R., "A reappraisal of Mount St. Helens ash clusters depositional model from experimental observation," J. Volcanol. Geotherm. Res. **59**, 253–260 (1994).

Schumacher, R. and Schmincke, H.-U., "Models for the origin of accretionary lapilli," Bull. Volcanol. **56**, 626–639 (1995).

Sparks, R. S. J., Bursik, M. I., Carey, S. N., Gilbert, J. S., Glaze, L. S., Sigurdsson, H., and Woods, A. W., *Volcanic Plumes* (John Wiley, New York, 1997), p. 574.

Steinke, I., Möhler, O., Kiselev, A., Niemand, M., Saathoff, H., Schnaiter, M., Skrotzki, J., Hoose, C., and Leisner, T., "Ice nucleation properties of fine ash particles from the Eyjafjallajökull eruption in April 2010," Atmos. Chem. Phys. **11**, 12945–12958 (2011).

Taddeucci, J., Scarlato, P., Montanaro, C., Cimarelli, C., Del Bello, E., Freda, C., Andronico, D., Gudmundsson, M. T., and Dingwell, D. B., "Aggregation-dominated ash settling from the Eyjafjallajökull volcanic cloud illuminated by field and laboratory high-speed imaging," Geology **39**(9), 891–894 (2011).

Telling, J. and Dufek, J., "An experimental evaluation of ash aggregation in explosive volcanic eruptions," J. Volcanol. Geotherm. Res. **209-210**, 1–8 (2012).

Telling, J., Dufek, J., and Shaikh, A., "Ash aggregation in explosive volcanic eruptions," Geophys. Res. Lett. **40**(10), 2355–2360, https://doi.org/10.1002/grl.50376 (2013).

Van Eaton, A. R., Muirhead, J. D., Wilson, C. J. N., and Cimarelli, C., "Growth of volcanic ash aggregates in the presence of liquid water and ice: An experimental approach," Bull. Volcanol. **74**(9), 1963–1984 (2012).

Wilson, L. and Huang, T. C., "The influence of shape on the atmospheric settling velocity of volcanic ash particles," Earth Planet. Sci. Lett. **44**, 311–324 (1979).